Electronic Supplementary Material (ESI) for Physical Chemistry Chemical Physics.

Supporting Information

Phase Separation Mechanism for a Unified Understanding of Dissipative Pattern Formation in a Liesegang System

Masaki Itatani,[a] Qing Fang,[b] István Lagzi,[c,d] , and Hideki Nabika[*b]

[a] Graduate School of Science and Engineering, Yamagata University, 1-4-12, Kojirakawa, Yamagata 990-8560, Japan

[b] Faculty of Science, Yamagata University, 1-4-12, Kojirakawa, Yamagata 990-8560, Japan

[c] Department of Physics, Budapest University of Technology and Economics, Budafoki út 8, Budapest 1111, Hungary

[d] MTA-BME Condensed Matter Physics Research Group, Budapest University of Technology and Economics, Budafoki út 8, Budapest 1111, Hungary

Corresponding author[*]: E-mail: nabika@sci.kj.yamagata-u.ac.jp, Tel. & Fax: +81-23-628-4589

Table of Contents

1 Experimental procedure for preparation of 11-mercaptoundecanoic acid (MUA-Au NPs)

1.1 Reagents and instruments

Hydrogen tetrachloroaurate (III) tetrahydrate ($HAuCl_4 \bullet 4H_2O$, 99.0%), Trisodium citrate dihydrate ($C_6H_5Na_3O_7 \bullet 3H_2O$, Cit), 0.01 M Sodium hydroxide solution (NaOH, factor (20 °C) = 1.0), Agarose (fine powder) as a gel medium, and Bromo Thymol Blue solution (BTB, 0.04 w/v%) were purchased from FUJIFILM Wako Pure Chemical Industry (Japan). 11-Mercaptoundecanoic acid (MUA, 95%) was purchased from Sigma-Aldrich (USA). Hydrochloric acid (HCl, 35%) was purchased from Nacalai Tesque Industry (Japan). All reagents were used without further purification. Ultraviolet-visible (UV-vis) and Fourier transform-infrared spectrometer (FT-IR), Transmission electron microscopy (TEM), and Dynamic light scattering (DLS) measurements were performed using a JASCO V630, a Thermo Fisher Scientific Nicolet 6700, a JEOL JEM-2100F at 200 kV, and an Otsuka electronics ELS-Z2M. The pH measurement was performed by using a pH meter (HORIBA F-51) with a pH electrode (HORIBA 9618S-10D). Optical microscopy and microspectrophotometry (MSP) measurements are carried out using an OLYMPUS BX-51 and a HAMAMATSU PMA-12. All pattern formation experiments were performed in glass test tubes (∅ = 10 mm). The formed patterns were observed using the same microscope as the above. Image analysis such as a line profiling and making grayscale images was performed using Image J software.

1.2 Synthesis of 11-mercaptoundecanoic acid (MUA-Au NPs)[1]

$HAuCl_4$ aq. soln. (250 mM, 400 µL) was added to ultra-purified water (99.6 mL) that is beforehand boiled by heating at 250 °C with stirring at 600 rpm. Immediately after it, Cit aq. soln, (38.8 mM, 10 mL) was added to the above $HAuCl_4$ aq. soln. and kept heating and stirring for 5 min. Subsequently, heating was stopped, and only stirring was kept for 60 min at room temperature. This mixture was then centrifugated at 15000 rpm for 30 min and redispersed by ultra-purified water. In the previous processes, dispersion of Au NPs stable by Cit (Cit-Au NPs) was prepared. Also, we prepared a NaOH aq. soln. (0.20 M, 10 mL) with dissolving MUA (moral ratio; added $HAuCl_4$:MUA = 1:5) by heating at 40 °C with stirring at 600 rpm for 30 min, where MUA was neutralized (deprotonated) at this basic condition. Subsequently, this basic MUA aq. soln. was added to the Cit-Au NPs dispersion with stirring at 300 rpm and keeping stirring at 25 °C at least 12 h to modify the surface of Cit-Au NPs with MUA molecules (Figure S1). After the modification, this mixture was centrifugated at 15000 rpm for 30 min and redispersed by ultra-purified water. The centrifugation was then repeated with the same condition and redispersed by ultra-purified water (1-2 mL). This obtained MUA-Au NPs dispersion was stored at 5 °C. Also, we used up this dispersion within a week to keep it fresh.

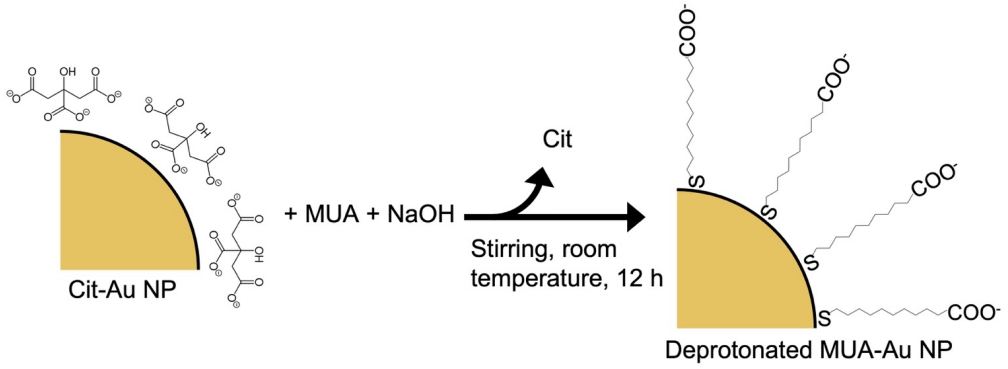

Figure S1. Scheme of synthesis of MUA-Au NPs.

1.3 Characterization of MUA-Au NPs

1.3.1 Ultraviolet-visible (UV-vis) and Fourier transform-infrared spectrometer (FT-IR) measurements

To evaluate the synthesis and modification of Cit- and MUA-Au NPS, we performed UV-vis measurement. We used Cit-Au NPs after purification by the centrifugation processes. Also, MUA-Au NPs after the set of centrifugations and redispersion process was used. The concentration of dispersion was decided by an extinction intensity of localized surface plasmon resonance (LSPR) peak around 520-530 nm.[2] In briefly, the concentration was calculated by the following relationships:

$$ln\varepsilon = klnD + a \quad (1)$$

$$Extinction\ intenisty = \varepsilon lC \quad (2)$$

where ε, D, l, and C are the extinction coefficient in $M^{-1}cm^{-1}$, the core diameter of the nanoparticles in nm the optical path length in cm, and the concentration in M. Also, k and a is the coefficient obtained by the fitting to eq. (1). In this study, we used the value set obtained in the previous study.[2] Furthermore, we also performed FT-IR measurement to evaluate the modification by MUA molecules and deprotonated in the basic condition. The purified Cit-Au NPs and MUA-Au NPs were used, in which the former one was vacuum dried, while the letter one was reprecipitated by EtOH and then vacuum dried. After the characterization of the synthesized particles is complete, we investigated the behavior of pH-induced aggregation of MUA-Au NPs in an agarose gel (0.20 w/v%) by UV-vis measurement. At first, an agarose powder was roughly dissolved in ultra-purified water by heating in a microwave oven, and then it was heated on a hot stirrer at 90 °C with stirring at 150 rpm to complete dissolving. After that, the concentrated MUA-Au NPs dispersion was added to this hot sol to be the final concentration of MUA-Au NPs 2.0 nM. This mixture was cooled at room temperature and the crude heat was removed. Just before gelation, this mixture was poured into the measurement cell (10×10 mm) and mixed with a prescribed concentration of HCl to prepare MUA-Au NPs-doped gels under different pH conditions. These samples were gelation at 18 °C for 30 min. Then, we performed UV-vis measurement.

1.3.2 Transmission electron microscopy (TEM) measurement

We used the purified Cit-Au NPs and MUA-Au NPs for TEM measurement. To prepare the samples for TEM measurement, 10 μL of dispersion was doped on a grid (Okenshoji, ELS-C-10) and dried at room temperature.

1.3.3 pH titration[3]

The pH titration was performed to investigate pK_a of the synthesized MUA-Au NPs. Before, the titration, we prepared the mixture of MUA-Au NPs and NaOH with a total volume of 10 mL, in which the final concentrations of MUA-Au NPs and NaOH were 1.0 nM and 1.0×10^{-2} M. For the titration, HCl aq. soln. (10 mM) was used. The titration was performed at room temperature with an *in-situ* pH measurement. The pH value was read after stirring for 5 min for each drop of HCl aq. soln. to allow sufficient time for each chemical process to reach the equilibrium state.

1.3.4 Dynamic light scattering (DLS) measurement

To investigate the aggregation kinetics of MUA-Au NPs, we carried out DLS measurement. There were two ways to measure it. At first, to obtain simple information on aggregation responsiveness to pH, we prepared a mixture of MUA-Au NPs (fixed 2.0 nM) with HCl (prescribed concertation) and measured a hydrodynamic radius against different pH values by DLS measurement 180 min after mixing of MUA-Au NPs and HCl. On the other hand, to obtain detailed information on aggregation kinetics, we performed DLS and pH measurements of change over time. The mixed solutions ([MUA-Au NPs] = 1.0 nM and [HCl] = 1.0×10^{-4}, 2.0×10^{-4}, and 1.0×10^{-3} M) were used for this measurement. All procedure in this section was performed at room temperature.

1.4 Patten formation by pH-induced aggregation of MUA-Au NPs

The NaOH solution (1.0×10^{-4} M) was mixed with MUA-Au NPs dispersion to be total volume 10 mL and the concentration of MUA-Au NPs desired. Subsequently, the agarose powder was added to this mixed solution at 0.20 w/v% and heated in a microwave oven to dissolve it. The solution was then immediately heated at 90 °C for 3 min with stirring at 150 rpm. Finally, heating with microwave oven again to dissolve agarose completely. This hot agarose sol was poured into a glass test tube to a height of 120 mm, and stood at 18 ± 0.5 °C for 3 h for complete gelation. Afterward, an HCl aq. soln. with prescribed concentration was poured on the top of the gel (Figure S2). The H^+ invading into the gel with diffusion began immediately, and a pH gradient with a diffusion gradient of H^+ was formed. In all conditions of pattern formation, the system was kept in a thermostat at 18 ± 0.5 °C, and the duration of pattern formation was fixed at 2 weeks. After the pattern formation, HCl aq. soln. was removed from the top of the gel. Then, the obtained sample was observed using microscopy measurement.

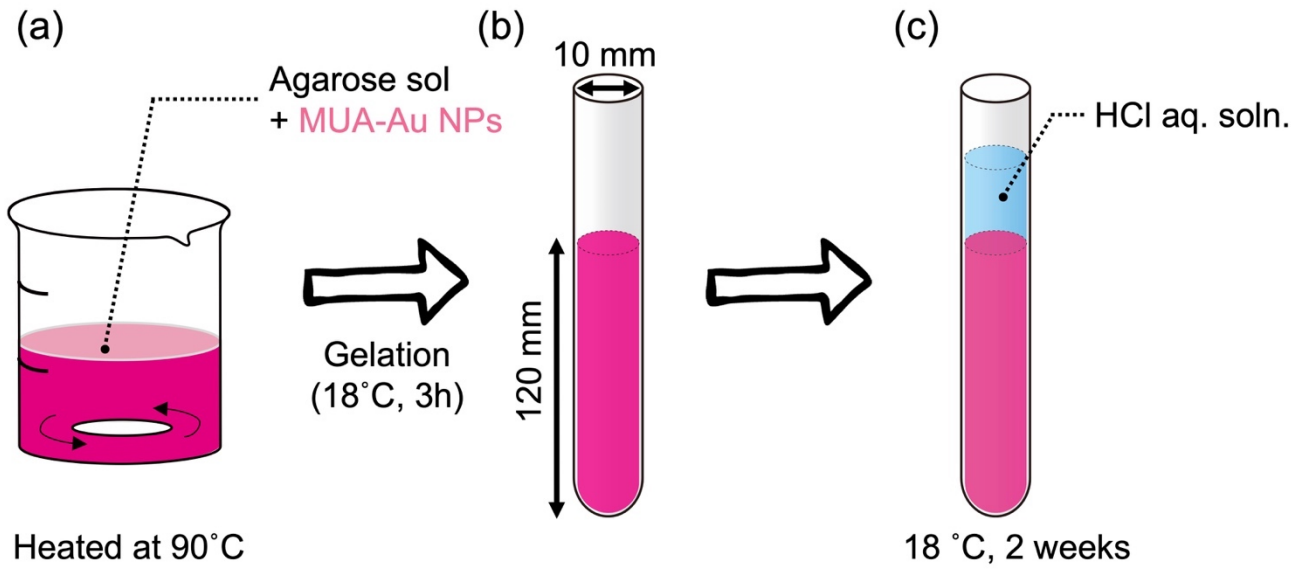

Figure S2. Illustration of experimental procedure of pattern formation in MUA-Au NPs aggregation system. (a) Preparation of agarose sol doped with MUA-Au NPs. (b) Making the agarose gel in a test tube. (c) Initiation of pattern formation by pouring HCl aq. soln. on the top of the gel.

1.5 Image analysis

We carried outline profile analysis for the obtained images of pattern formation. Before line profiling, original images were converted to grayscale images using the Image J software. Then, the line profile was carried out from an interface between the HCl reservoir and the gel. The result was output as a gray value for spatial coordinates toward the bottom of the gel. For our setting, the gray value was represented with a range from 0 to 255, where 0 and 255 corresponded to black (dark color in original images) and white (light color in original images). Then, we obtained the inverted gray value (IGV) by reversing this relationship using the following method.

$$IGV = 255 - gray\ value \quad (3)$$

The higher value, the color of the analyzed area is close to black in IGV, namely an aggregation region indicates the higher IGV.

1.6 Visualization of H^+ diffusion front with Bromo Thymol Blue (BTB)

Basically, the procedures of the gel preparation and the pattern formation were according to the description in section 1.4. However, we added BTB solution instead of MUA-Au NPs solution to be the concentration 8.0×10^{-4} w/v%.

1.7 pH-induced aggregation of MUA-Au NPs in rectangular agarose gel

We made the rectangular mold by sandwiched a silicone rubber sheet that hollow out inside as rectangular-shaped with two glass plates. Based on the same procedure as described in section 1.4, the gel pre-doped MUA-Au NPs was prepared in this mold. After the gelation, the pattern formation was carried out with the HCl diffusion. The obtained pattern was observed using the optical microscope equipped with a microspectrophotometer.

2 Results and Discussion

2.1 UV-vis and FT-IR measurements

Figure S3a shows the result of UV-vis measurement for a pre-modification (Cit-Au NPs) and a post-modification (MUA-Au NPs). The LSPR peak shifted from 518 nm to 528 nm after the modification by MUA molecules. Since such red-shift was also observed in the previous study for the synthesis of MUA-Au NPs,[1] therefore, it was suggested that the modification was succeeded. Also, the FT-IR spectrum showed stronger evidence for the modification (Figure S3b). The blue region (i) and (ii) corresponds to the absorbance of S-H stretching and COOH stretching. Since the broad peak of absorbance disappeared in the region (i) through the modification, we found that the S-H bond was replaced by the Au-S bond. Furthermore, the strong sharp peak in region (ii) also disappeared after the modification, indicating that the COOH was deprotonated and formed COO^-. Therefore, we found that the synthesis of deprotonated MUA-Au NPs was succeeded from above the results of UV-vis and FT-IR measurements.

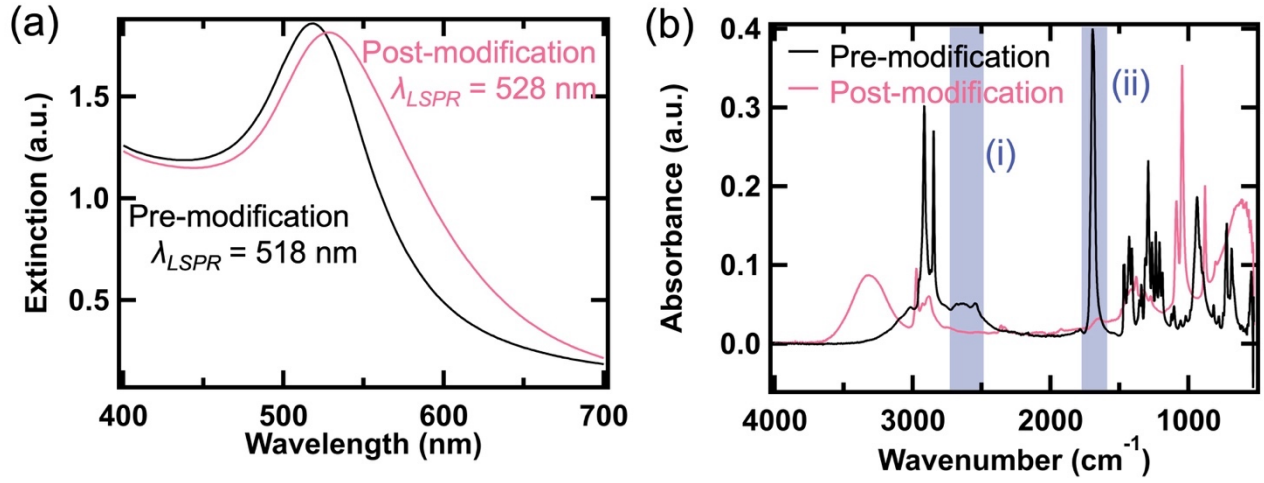

Figure S3. (a) UV-vis and (b) FT-IR spectra for the pre-modification NPs (synthesized Cit-Au NPs) and the post-modification MUA sodium.

2.2 TEM measurement

TEM measurement was performed for Cit-Au NPs (Figure S4a) and MUA-Au NPs (Figure S4b). While the average size of Cit-Au NPs was 13 ± 3.6 nm, MUA-Au NPs was 15 ± 3.5 nm, where the average size was calculated from at least the particle number of 100. The size was almost unchanged before and after the modification.

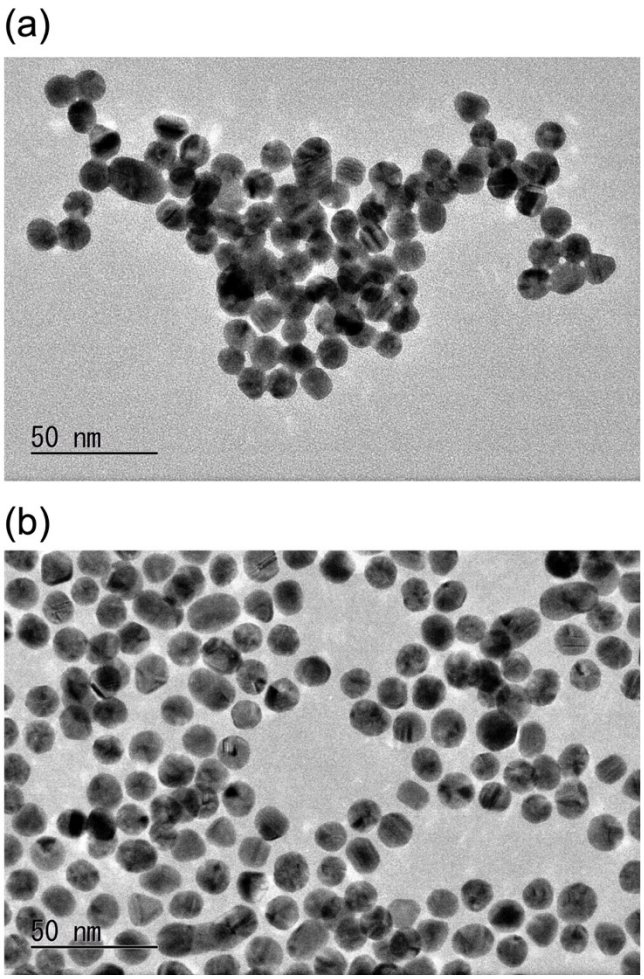

Figure S4. TEM micrographs of (a) Cit-Au NPs and (b) MUA-Au NPs. The average particle sizes of each NPs are 13 ± 3.6 nm (Cit-Au NPs) and 15 ± 3.5 nm (MUA-Au NPs).

2.3 pH titration

Figure S5a shows a titration curve of the full range of titration HCl volume. We can see the first plateau until around the $V_{titration}$ = 7500 µL, corresponding to the titration of excess hydroxide ions. Then, the second plateau appears between two broken lines in Figure S5b, resulting from the titration of carboxylates on the MUA-Au NPs surface and buffering by them. According to the previous study,[3] the pK_a of MUA molecules on the AU NPs surface was estimated from the pH halfway through the second plateau. Thus, the pK_a of our synthesized MUA-Au NPs was 6.8. This value is close to the other study of synthesizing MUA-Au NPs.[4]

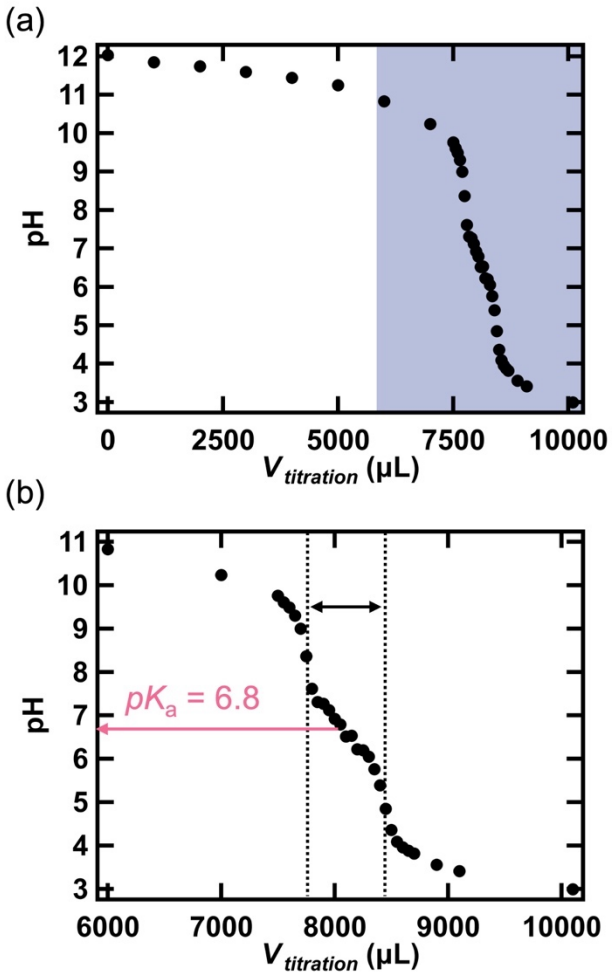

Figure S5. Experimental titration curve of basic MUA-Au NPs aq. soln. ([MUA-Au NPs] = 1.0 nM, 10 mL) with HCl aq. soln. ([HCl] = 1.0×10^{-2} M). (a) The range of all titration volume and (b) magnification of blue region in (a).

2.4 DLS measurement

Figure S6 shows a relationship between hydrodynamic radius and pH values 180 min after mixing MUA-Au NPs and HCl. The radius began increasing slightly below pK_a 6.8 but increased dramatically below pH 4. Therefore, it was found that a pH-induced aggregation occurred around pH 4.

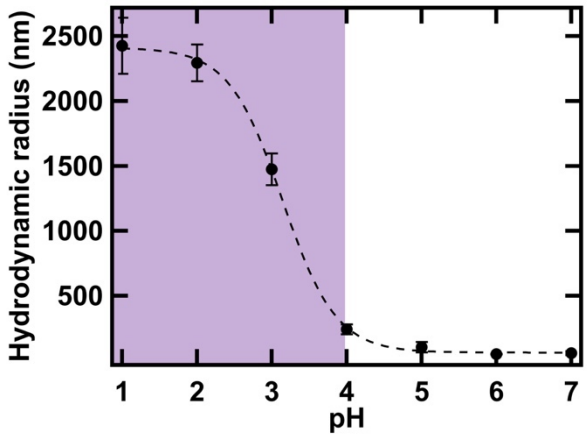

Figure S6. Variation of hydrodynamic radius of MUA-Au NPs as the function of pH, which was measured by DLS ([MUA-Au NPs] = 2.0 nM). The purple region indicates the pH range of aggregating MUA-Au NPs. Measurements were carried out 180 minutes after mixing with HCl.

Also, the time course of pH and the mean particle size estimated by DLS measurements were shown in Figure S7. When the concentration of HCl is 1.0×10^{-4}, the pH value is almost constant around 7 from 0 h to 24 h (Figure S7a▲). On the other hand, the particle size increases slightly (Figure S7a●), namely, MUA-au NPs aggregated slowly in this HCl concentration. Although the pH value is also constant around 4 in the case of [HCl] = 2.0×10^{-4}, the particle size increases linearly from about 50 nm to 450 nm (Figure S7b). The rate of increase is greater for [HCl] = 2.0×10^{-4} than for [HCl] = 1.0×10^{-4}. When the concentration of HCl is further increased ([HCl] = 1.0×10^{-3}), the particle size increases dramatically until 5 h and becomes plateau, while the pH value was fixed at around 3 (Figure S7c). Therefore, it was found that the case of [HCl] = 2.0×10^{-4} behaved medium speed aggregation, and the [HCl] = 1.0×10^{-3} showed fast speed aggregation. Since the pattern formation was carried out at around pH 4-5 in this study, we guessed the pH-induced aggregation progressed with the medium speed aggregation.

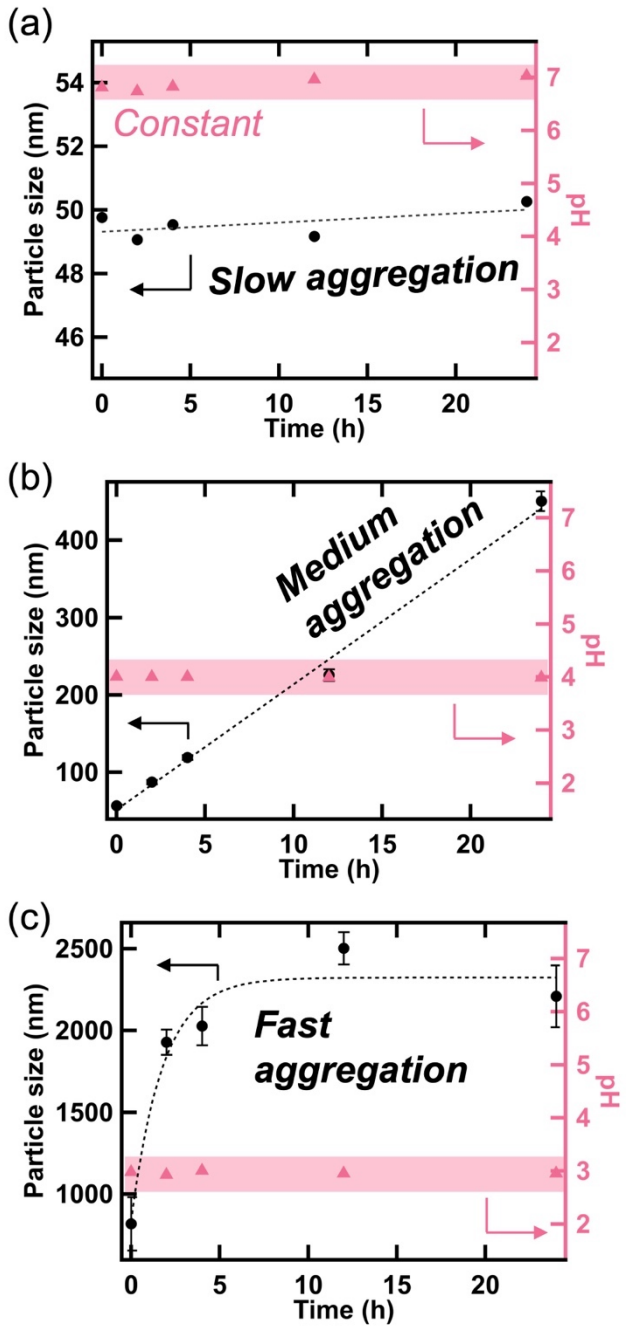

Figure S7. Changes in particle size (left black axis) and pH (right red axis) in MUA-Au NPs aq. soln. (1.0 nM) as a function of time and dependence on the concentration of adding HCl aq. soln.: (a) [HCl] = 1.0×10^{-4} M, (b) 2.0×10^{-4} M, and (c) 1.0×10^{-3} M. Particle size was measured by DLS.

2.5 UV-vis measurement with different pH in agarose gel

Figure S8a shows the color changes of agarose gels contained with MUA-Au NPs with different pH values from 2 to 7, which was adjusted by mixed with HCl. Until pH was 3, the color remained red, but it was changed to purple at pH 7. To discuss this pH responsibility to pH, we performed UV-vis measurement (Figure S8b). As a result, LSPR peak intensity around 530 nm increases when pH decreases until 3. Also, this peak is red-shifted and broadening in the case of pH 2. The previous study reported that the LSPR peak just increased if nanoparticles aggregated weakly, then the peak was red-shifted if they aggregated strongly.[5] Therefore, it was suggested that MUA-Au NPs were aggregated weakly between pH 3 to 7. This pH range corresponded to the condition of pattern formation. Therefore, it was found that the pattern was formed via the weak pH-induced aggregation and following medium speed aggregation to form μm scale aggregates shown in Figure 1d.

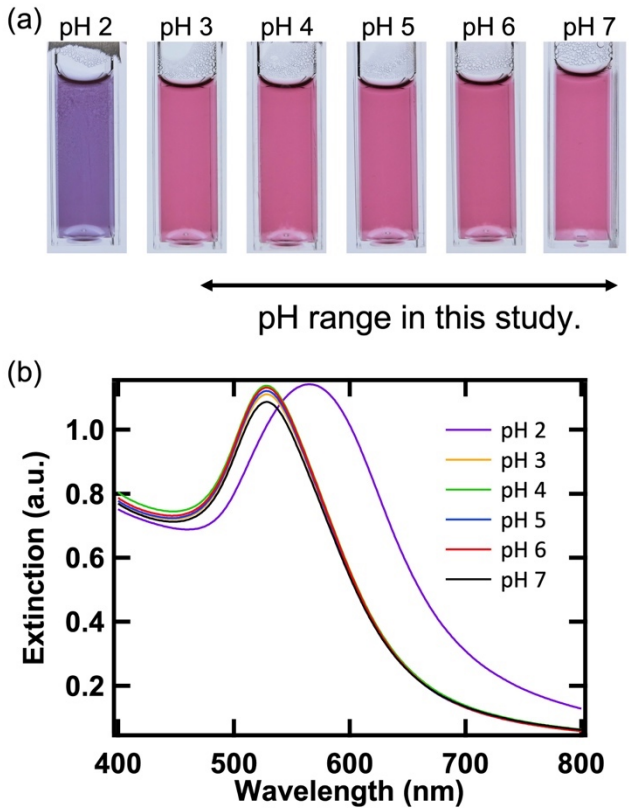

Figure S8. (a) Color changes of agarose gels doped with MUA-Au NPs 30 min after the pH is adjusted from 2 to 7 by HCl aq. soln. ([agarose] = 2.0 w/v% and [MUA-Au NPs] = 2.0 nM). (b) UV-vis spectra in (a).

2.6 Visualization of H^+ diffusion front with BTB

Figure S9a-b shows the color changes of BTB indicator with the diffusion of H^+, where the color of BTB changes from blue to yellow when pH values change from 7.6 to 6.0. Therefore, the pH of the region showing yellow means below 6.0, in which this value is the trigger of the aggregation (Figure S6). After 48, the yellow front reached x = 60 mm (Figure S9d). In this study, there was the region of pattern within 30 mm. Therefore, H^+ diffused enough under this study's condition (2 weeks).

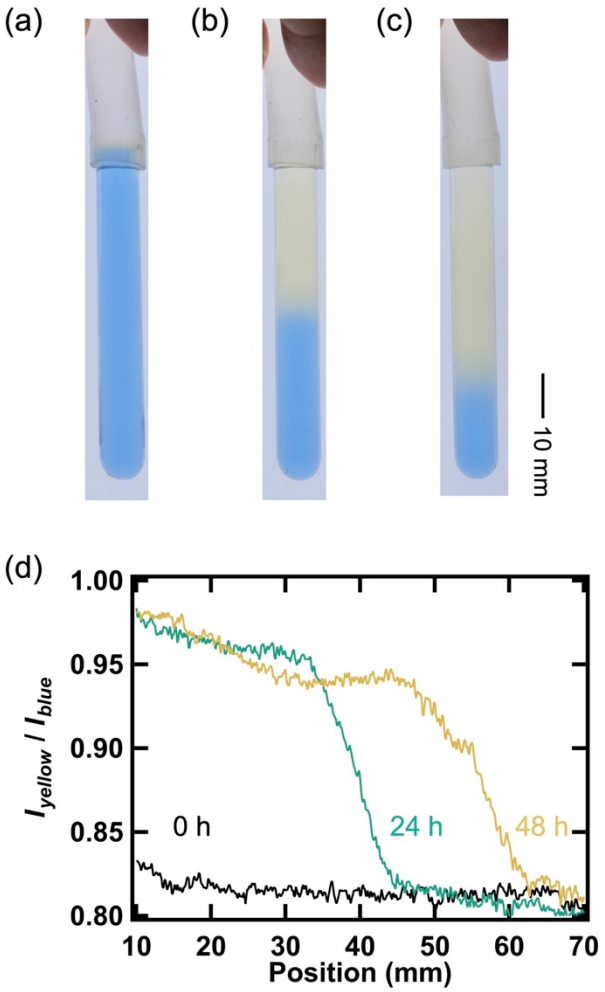

Figure S9. Visualization of H^+ diffusion front by BTB ([agarose] = 0.20 w/v%, $[HCl]_0 = 1.0\times10^{-4}$ M, and $[BTB]_0 = 8.0\times10^{-4}$ w/v%): (a) 0 h, (b) 24 h, and (c) 48 h. (d) Ratio of color intensity between yellow and blue as a function of position measured from the interface between the HCl reservoir and the gel.

2.7 Evaluation of elution of MUA-Au NPs after pattern formation by UV-vis measurement

After the typical pattern formation, the red color near the top of the gel became pale (Figure 1a). When aggregation occurs, the color becomes dark red (or purple). Therefore, such color decreasing might be caused by other facts. Figure S10 is the UV-vis spectra of the removed HCl reservoirs after the pattern formation with different HCl concentrations. The LSPR peak of MUA-Au NPs around 530 nm was observed. Therefore, MUA-Au NPs eluted from the gel to the reservoir during the pattern formation, it was found that the above color changing was caused by the elution.

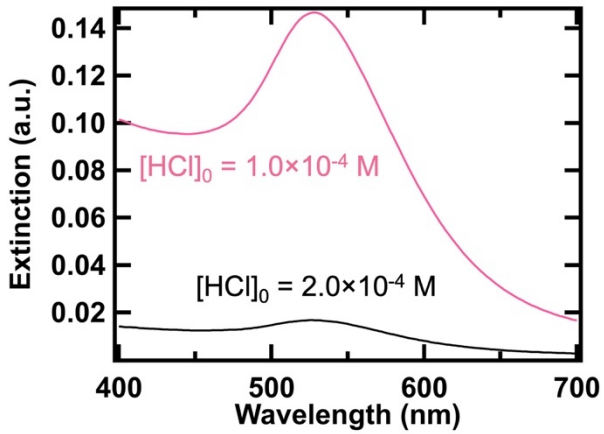

Figure S10. (a) UV-vis spectra of HCl reservoir after pattern formation (2 weeks) with the different concentrations of HCl reservoir: $[HCl]_0 = 1.0\times10^{-4}$ M (red) and 2.0×10^{-4} M (black).

2.8 Investigation of aggregation state in agarose gel by microspectrophotometry (MSP) measurement

Figure S11 shows UV-vis spectra at some positions in the obtained pattern measured by MSP. The black, red, and purple lines indicate positions where an out region of the H^+ diffusion range, a band region, and a depletion (inter-band) region. At the band, the LSPR peak increased than the out of diffusion, namely MUA-Au NPs was aggregated in the band region. On the other hand, the LSPR peak intensity at the depletion region decreased than the band region. Therefore, it was suggested that the concentration of MUA-Au NPs decreased and/or the aggregation did not progress at the depletion region.

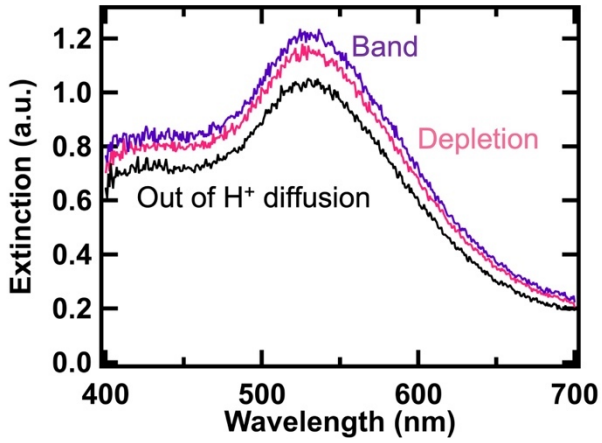

Figure S11. UV-vis spectra measured by MSP at the position of the band (purple) and depletion (red) in gel sample such as Figure 1a. The black spectrum is obtained out of the H^+ diffusion region.

2.9 pH-induced aggregation of MUA-Au NPs in rectangular agarose gel

Figure S12a shows the pH-induced aggregation by the H^+ diffusion in the agarose gel. Since the initial concentration of HCl ($[HCl]_0 = 2.0\times10^{-4}$ M) was higher than the typical condition in this study ($[HCl]_0 = 1.5\times10^{-4}$ M), the MUA-Au NPs was strongly aggregated (purple color, region 1) near the gel top. However, the concentrated red color appeared below the region 1 (region 2). Further below, the original red color was observed (region 3), meaning MUA-Au NPs were dispersed. For each region, we performed MSP measurement (Figure S12b). Similar to the results of early UV-vis measurements, the LSPR peak intensity increased from region 3 to region 2, because MUA-Au NPs aggregated weakly (transition (i)). Furthermore, the peak became broadening and red-shifted at region 1 (transition (ii)). The obtained pattern in this study (Figure 1) showed only original and concentrated colors. Therefore, it was strongly supported that the pattern formation did not include the strong aggregation process in this study.

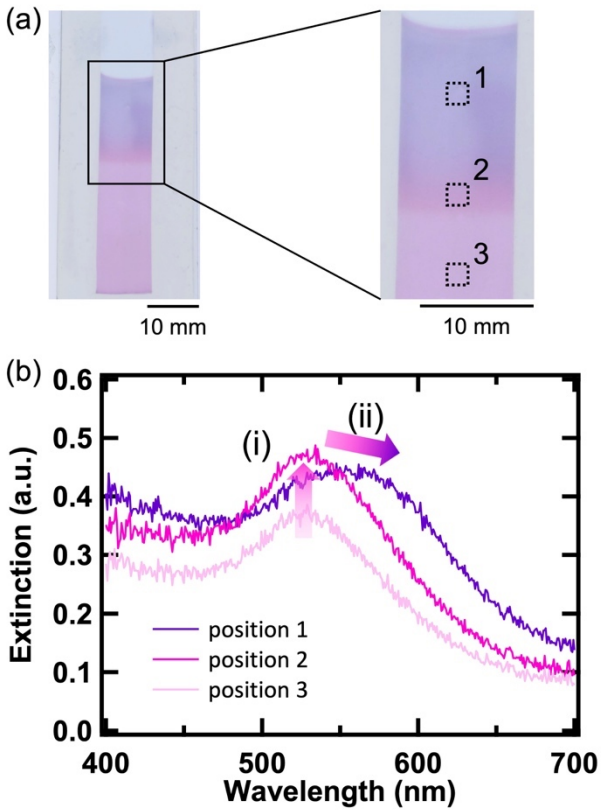

Figure S12. (a) Aggregation of MUA-Au NPs in the rectangular agarose gel by directional diffusion of HCl ([agarose] = 0.20 w/v%, $[HCl]_0 = 2.0\times10^{-4}$ M, and $[MUA\text{-}Au\ NPs]_0 = 4.0$ nM). (b) UV-vis spectra measured by MSP at the position from 1 to 3 in (a).

2.10 Pattern formation with different initial MUA-Au NPs concentrations ([MUA-Au NPs]$_0$)

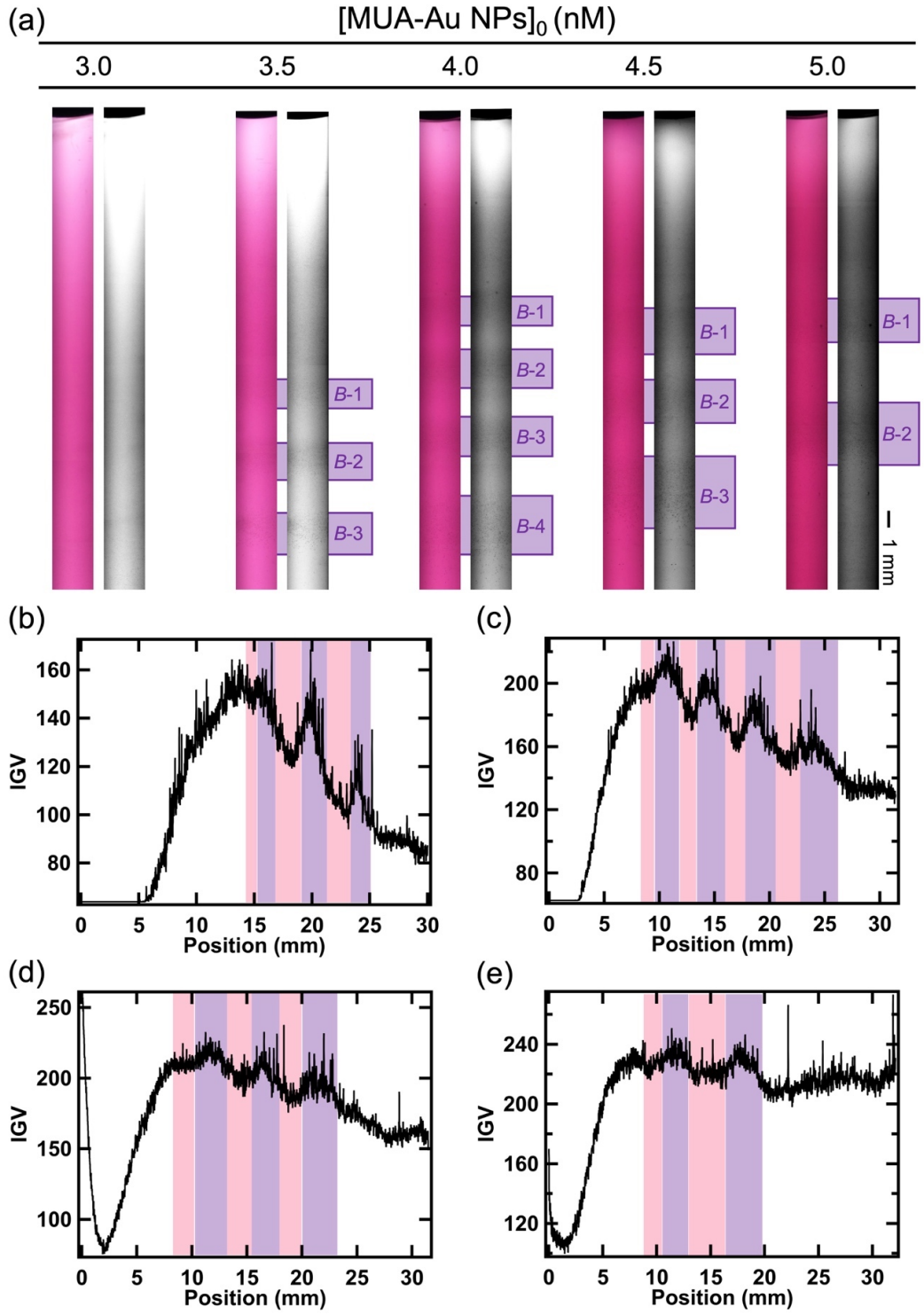

Figure S13. (a) Pattern formation with the different initial MUA-Au NPs concentrations ([agarose] = 0.20 w/v% and [HCl]$_0$ = 1.5×10^{-4} M). Left and right images in each set are original color and grayscale. Line profile in different [MUA-Au NPs]$_0$: (b) 3.5 nM, (c) 4.0 nM, (d) 4.5 nM, and (e) 5.0 nM. These profiles were obtained from grayscale images.

2.11 Pattern formation with different initial HCl concentrations ($[HCl]_0$)

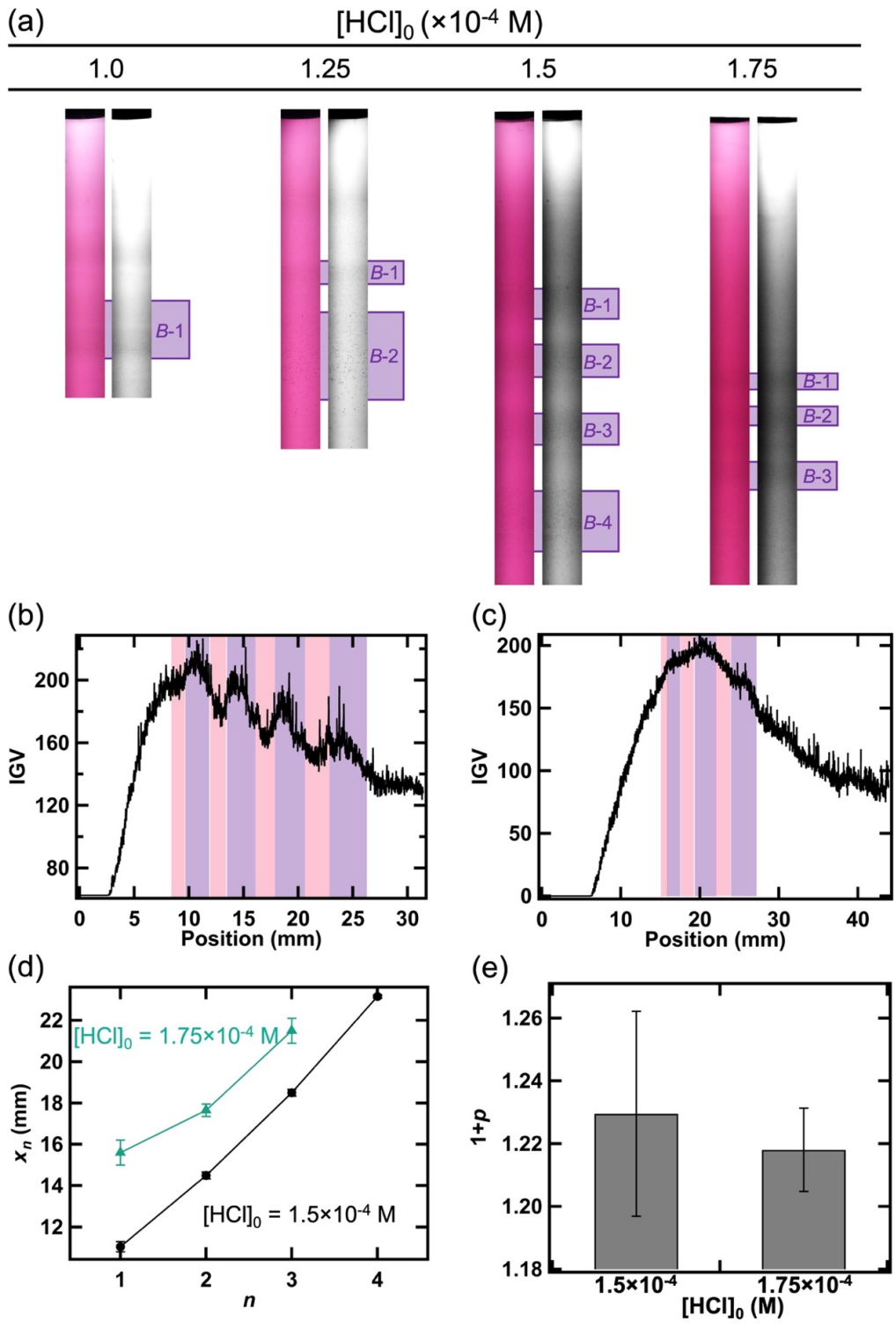

Figure S14. (a) Pattern formation with the different initial HCl concentrations ([agarose] = 0.20 w/v% and $[MUA\text{-}Au\ NPs]_0$ = 4.0 nM). Left and right images in each set are original color and grayscale. Line profile in different $[HCl]_0$: (b) 1.5×10^{-4} M and (c) 1.75×10^{-4} M. (d) Variation of band position (x_n) with band number (n) in different $[HCl]_0$ (●: 1.5×10^{-4} M and ▲: 1.75×10^{-4} M). (e) Relationship between spacing coefficient (p) and $[HCl]_0$.

3. Simulations based on numerical reaction-diffusion (RD) model

We constructed a numerical RD model coupled with the Cahn-Hilliard equation,[6-11] because the pattern formation driven by the pH-induced aggregation was possible to progress via phase separation mechanism. In our experiments, the following chemical processes was included in the pH-induced aggregation

Protonation: $n\mathrm{H^+}$ + Au NP-$(\mathrm{COO^-})_n$ → Au NP-$(\mathrm{COOH})_n$ (4)

Phase transition and separation: mAu NP-$(\mathrm{COOH})_n$ → $(\mathrm{Au\ NP})_m$ (5)

where -$(\mathrm{COO^-})_n$ and $(\mathrm{Au\ NP})_m$ are the MUA molecules on the Au NP surface and aggregates of MUA-Au NPs, respectively. Then, we expressed the above processes for simulation as

Protonation: A + Z → Z* (6)

Phase transition and separation: Z* → Z** (7)

Each species in Eqs. (6) and (7) corresponds to the chemical species in Eqs. (4) and (5). Based on these assumed processes, we constructed following RD equations, referring to past numerical studies for the post-nucleation models.[6-8]

$$\frac{\partial a}{\partial t} = D_a \frac{\partial^2 z}{\partial x^2} - 10kzPrt(x,t), \tag{8}$$

$$\frac{\partial z}{\partial t} = D_z \frac{\partial^2 z}{\partial x^2} - kzPrt(x,t), \tag{9}$$

where a and z are concentrations of A and Z, D_a and D_z are the diffusion coefficients of A and Z, respectively, and k is the rate constant of the protonation reaction. To consider the chemical amphipathic relationship between the number of MUA molecules per one MUA-Au NP surface and protons, we added the correction coefficient number (10) before $kzPrt(x,t)$ in eq. (8). The protonation progresses dramatically as shown in Figure S5. Therefore, the term for the protonation should be denoted using the sigmoid function. Then, the protonation function $Prt(x,t)$ was represented by the following sigmoid-type function:

$$Prt(x,t) = z\left(\frac{1}{1+e^{-\alpha(a(x,t)-K_a)}}\right), \tag{10}$$

where α and K_a are a coefficient that determines the degree of change and acidity constant. The eq. (10) represents that the Z* is accumulated at the position where A was diffused and increased. Also, α controlled the responsibility of the Z* production (meaning protonation) to the increase in A. In this study, we fixed α and K_a at 1.0 and 12. When the system becomes unstable by the increase in Z*, a phase separation of Z* into regions of high (z_h) and low concentrations (z_l) takes place, where the region with z_h means existence of Z** (aggregation). This process is denoted by the following Cahn-Hilliard equation with protonation source ($kzPrt(x,t)$) and noise (η_Z) terms:

$$\frac{\partial X}{\partial t} = -\lambda \frac{\partial^2}{\partial x^2}\left(\varepsilon X - \gamma X^3 + \sigma \frac{\partial^2 X}{\partial x^2}\right) + kzPrt(x,t) + \eta_{Z.} \tag{11}$$

Here X is the concentration of Z* shifted by $\overline{z^*} = (z_h + z_l)/2$ and scaled by $\widehat{z^*} = (z_h - z_l)/2$, such that $X = (z^* - \overline{z^*})/\widehat{z^*}$ is 1 for $z^* = z_h$ and X is −1 for $z^* = z_l$.The parameters λ and σ are the kinetic constant of the phase separation and surface energy, ε and γ are the characteristic constants. The ratio between λ and σ defines a characteristic timescale of the unstable region growing. Also, σ guarantees stability for perturbation, it

is typically set positive value (σ > 0). In this study, we used 0.5 and 0.8 for λ and σ. The values of ε and γ define a binodal boundary and a spinodal boundary. Also, we set ε was positive, namely, the phase separation was driven by the spinodal decomposition. Values of ε and γ were 1.0. The above parameters were fixed in all simulations. Since fluctuations are inherent in various chemical phenomena, we have taken their effects into account with a noise term (η_Z) that is defined by $\eta_Z = r\sqrt{kzPrt(x,t)}$ where r is uniformly distributed in $[-\eta, +\eta]$. We used 0.02 as this parameter. Also, the space grid-step Δx = 1 is employed on a 100×400 grid, and the time step Δt = 0.001 and total time steps t = 500000 are used. Furthermore, the initial conditions were set as represented below: $a(x = 0, t = 0) = a_0$, $a(x > 0, t = 0) = 0$, and $z(x, t = 0) = z_0$, where a_0 and z_0 are initial concentrations of A and Z. Also, we used no-flux boundary conditions at the end of the calculation space (100×400 grid) and Dirichlet boundary conditions at the boundary between the A reservoir and the area pre-doped with Z, namely $a(x = 0, t) = a_0$. All parameters were treated as dimensionless.

For simplicity, we gave explanation of phase transition and separation by using RD equations on spatially one-dimensional domains. These RD equations can be extended to spatially two-dimensional domains where the diffusion operator $\partial^2/\partial x^2$ is replaced by $\nabla^2 = \partial^2/\partial x^2 + \partial^2/\partial y^2$, which are consistent with our experiments.

Also, we carried out numerical simulation on MATLAB platform. Finite difference methods for spatial derivatives were used, where the relative spatial step sizes were small. We then implemented the fourth order Runge-Kutta method to the ordinary differential equations obtained from discretization of spatial derivatives for the reaction-diffusion equations. The temporal step size was chosen so small that stability conditions are satisfied to guarantee stable and reliable numerical solutions.[12, 13]

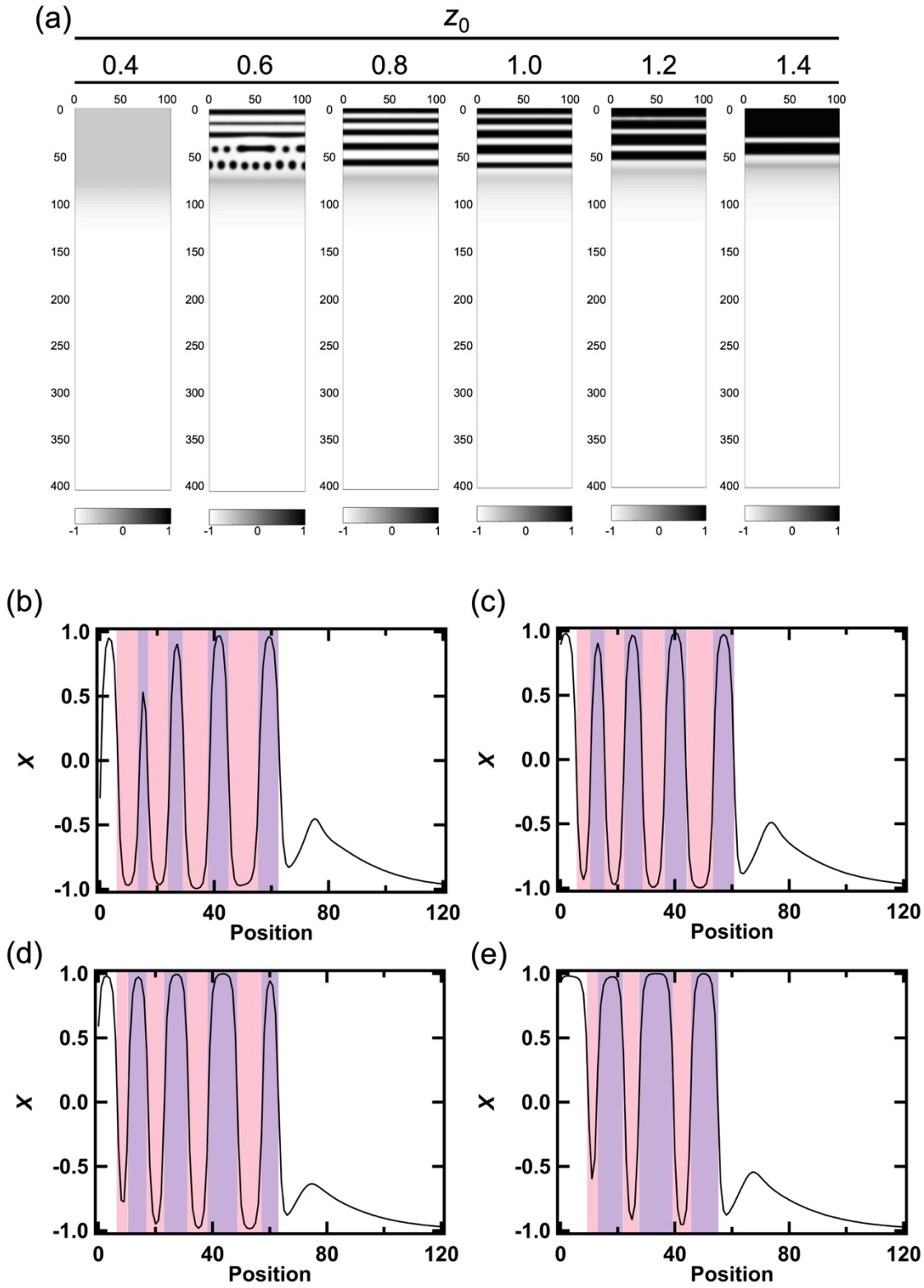

Figure S15. (a) Concentration distribution of X from RD simulation with different initial concentrations of Z (z_0) (t = 500000, a_0 = 60, D_a = 10, D_z = 1.0, α = 1.0, k = 1.0, K_a = 12, λ = 0.5, ε = γ = 1.0, σ = 0.8, η = 0.02). Line profile in different z_0: (b) 0.6, (c) 0.8, (d) 1.0, and (e) 1.2.

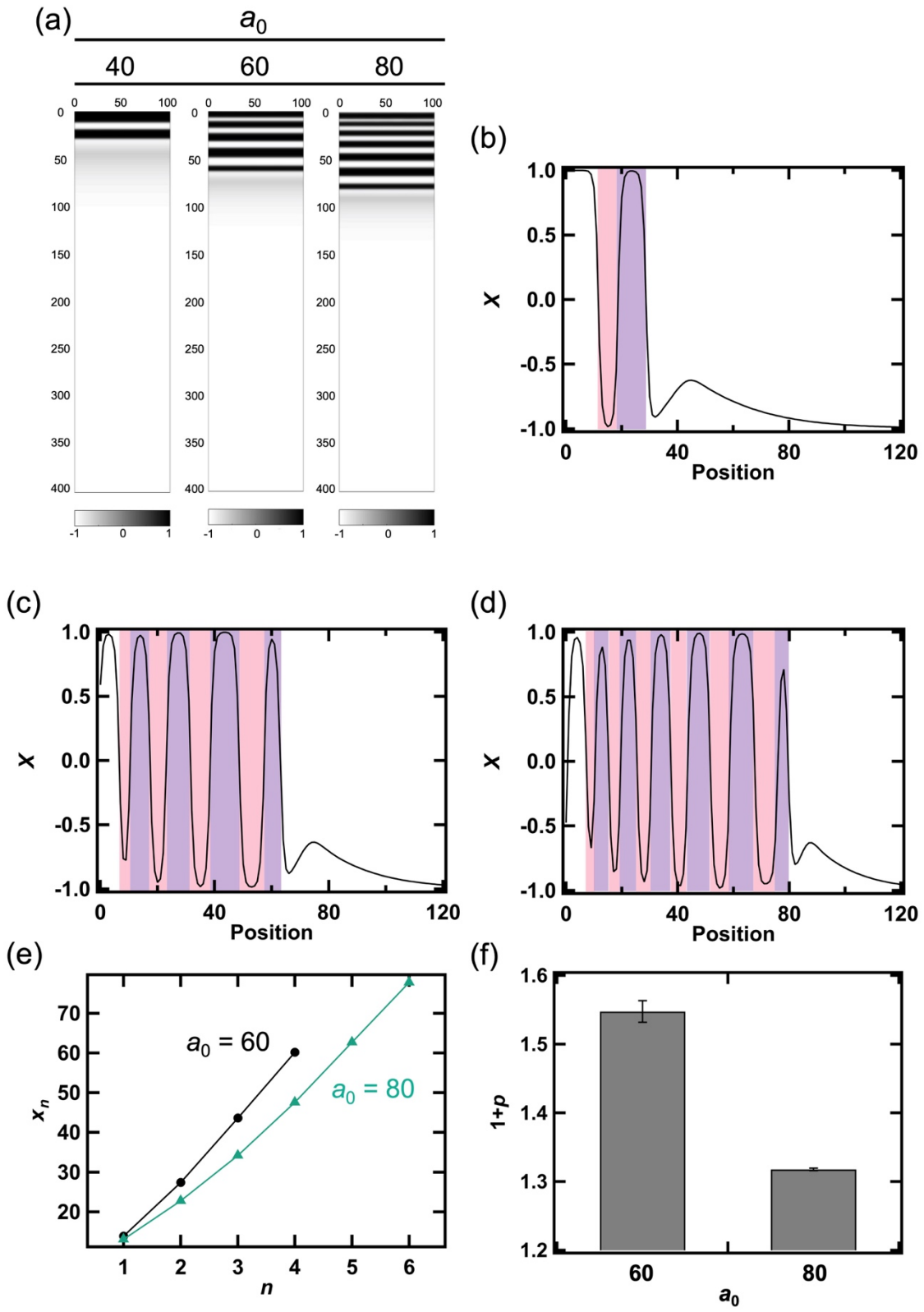

Figure S16. (a) Concentration distribution of X from RD simulation with different initial concentrations of A (a_0) (t = 500000, z_0 = 1.0, D_a = 10, D_z = 1.0, α = 1.0, k = 1.0, K_a = 12, λ = 0.5, ε = γ = 1.0, σ = 0.8, η = 0.02). Line profile in different a_0: (b) 40, (c) 60, and (d) 80. (e) Variation of x_n with n in different a_0 (●: 60 and ▲: 80). (e) Relationship between p and a_0.

4. References

1. J. Piella, N. G. Bastús and V. Puntes, *Chem. Mater.*, 2016, **28**, 1066-1075.
2. X. Liu, M. Atwater, J. Wang and Q. Huo, *Colloids and Surfaces B: Biointerfaces*, 2007, **58**, 3-7.
3. G. Charron, D. Hühn, A. Perrier, L. Cordier, C. J. Pickett, T. Nann and W. J. Parak, *Langmuir*, 2012, **28**, 15141-15149.
4. D. Wang, R. J. Nap, I. Lagzi, B. Kowalczyk, S. Han, B. A. Grzybowski and I. Szleifer, *J. Am. Chem. Soc.*, 2011, **133**, 2192-2197.
5. H. Nakanishi, A. Deák, G. Hólló and I. Lagzi, *Angew. Chem. Int. Ed.*, 2018, **57**, 16062-16066.
6. T. Antal, M. Droz, J. Magnin and Z. Rácz, *Phys. Rev. Lett.*, 1999, **83**, 2880-2883.
7. Z. Rácz, *Phys. A*, 1999, **274**, 50-59.
8. T. Antal, I. Bena, M. Droz, K. Martens and Z. Rácz, *Phys. Rev. E*, 2007, **76**, 046203.
9. J. W. Cahn and J. E. Hilliard, *J. Chem. Phys.*, 1958, **28**, 258-267.
10. J. W. Cahn, *Acta metall.*, 1961, **9**, 795-801.
11. P. C. Hohenberg and B. I. Halperin, *Rev. Mod. Phys.*, 1977, **49**, 435-479.
12. E. Hairer, G. Wanner, and S. P. Nørsett, *Solving Ordinary Differential Equations I - Nonstiff Problems*, Springer, 1993.
13. E. Hairer and G. Wanner, *Solving ordinary differential equations II*, Springer, 1996.